International Journal of Remote Sensing
Vol. 32, No. 23, 10 December 2011, 8053–8080

Taylor & Francis
Taylor & Francis Group

Inferring Greenland melt and refreeze severity from SeaWinds scatterometer data

BRANDON R. HICKS and DAVID G. LONG*
459 CB, Brigham Young University, Provo, UT, 84602, USA

(*Received 22 February 2010; in final form 30 August 2010*)

Two SeaWinds radar scatterometers operated in tandem for 9 months in 2003, enabling resolution of the diurnal cycle in Greenland. This dataset provides unprecedented temporal resolution for Ku-band scattering observations of snow and ice melt conditions. As a step towards improved radar-based melt intensity estimation, a simple Markov melt–thaw model is developed to estimate melt and refreeze indices. The melt indices model is evaluated with the aid of a simple geophysical–electromagnetic model and validated by comparing tandem SeaWinds observations against automated weather station data. The new approach is used to analyse the melt conditions over the Greenland ice-sheet in 2003. The strengths and limitations of the approach are considered.

1. Introduction

The Greenland ice-sheet profoundly influences the Earth's climate. The planet's solar radiation budget is directly affected by the albedo of the Greenland ice-sheet, which is strongly affected by the liquid water content in the snow – nearly 45% more incoming solar radiation is absorbed by wet snow than dry snow (Abdalati and Steffen 1995). Higher temperatures in Greenland cause increased duration and areal extent of the melt season, increasing the amount of the Sun's radiation that is absorbed, which in turn increases temperatures and melt. This positive feedback mechanism makes Greenland sensitive to subtle climate changes and an indicator of global climate change. Thus, understanding the processes that drive melt in Greenland is important in understanding climate.

The radar backscatter measured by scatterometers such as SeaWinds is very sensitive to the presence of liquid water (Kunz and Long 2006). This makes scatterometers very useful in detecting the onset of melt in snow and ice. As a result, a number of melt and ablation studies in Greenland have been conducted using active microwave sensors (Abdalati and Steffen 1997, Wismann 2000, Nghiem *et al*. 2001, Ashcraft and Long 2005, 2006a). However, these studies have focused primarily on melt detection – little has been done to explore the application of scatterometer data in understanding the amount of melting, termed 'melt intensity' or 'melt severity'. A limitation of these prior studies has been the limited temporal resolution of the scatterometer data.

During their tandem mission for nine months in 2003, the two SeaWinds scatterometers operating on QuikSCAT (Quick Scatterometer) and ADEOS II (Advanced

*Corresponding author. Email: long@ee.byu.edu

International Journal of Remote Sensing
ISSN 0143-1161 print/ISSN 1366-5901 online © 2011 Taylor & Francis
http://www.tandf.co.uk/journals
http://dx.doi.org/10.1080/01431161.2010.532174

Earth Observing Satellite 2) provided unprecedented temporal and spatial sampling of the Greenland ice-sheet. This Ku-band radar backscatter dataset is thus a valuable resource in studying melt–freeze cycles over the ice-sheet.

As a step towards improved estimation of melt severity, in this article we use the improved temporal resolution of the tandem SeaWinds mission to study the detection of melt and estimation of melt severity over the Greenland ice-sheet from images of Ku-band normalized radar cross-section σ^o. The new melt detection method developed in this article classifies three ice-states: frozen, melting and refreezing. The method combines a parameterized layered melt model with a one-step Markov state detection model to classify the ice in these possible states. We further extend the melt detection model to provide melt and refreeze severity indices, which provide simple measures of melt and refreeze significance at each location, that is, melt severity. The method provides seasonal estimates of melt onset, refreeze onset, melt season length, and seasonal melt severity across the ice-sheet.

To help explain and validate the radar measurements and indices, a very simple one-dimensional geophysical–electromagnetic model is used. Backscatter measurements and derived indices are compared to *in situ* temperature and radiation data at the ETH Swiss Camp automatic weather station (AWS) maintained by the Greenland Climate Network (GC-NET) (Steffen *et al*. 1996). The melt severity index (MSI) and ice-state classification correlate well with *in situ* data. An analysis of the melt onset, refreeze onset, and melt season length and a comparison of the seasonal melt severity with an ice facies map created using Seasat-A Scatterometer (SASS) data by Long and Drinkwater (1994) is also given. The tandem SeaWinds images are generated using the Scatterometer Image Reconstruction (SIR) algorithm (Early and Long 2001) with local time-of-day temporal filtering (Hicks and Long 2006). The resulting image set, providing three nearly uniformly spaced temporal samples per day over the entire ice-sheet, enables the resolution of the diurnal cycle.

Section 2 describes the models and algorithms used in this study. Section 3 discusses the application of the models and algorithms to the data and presents key results, while §4 concludes.

2. Method

This study attempts to improve melt detection and estimate melt severity by applying a model-based technique that facilitates the detection of liquid water in the snow-pack, as well as the distinction of melt and refreeze phases. This section describes the model and the algorithm used to detect and estimate melt. A simple simulation is used to verify key aspects of the melt detection and severity estimation model.

2.1 *Layered melt model*

Distinguishing melting snow from frozen snow can be difficult due to the gradual nature of melting. Melt occurs as liquid water becomes present in initially dry snow. As the liquid content increases, the physical and electrical properties of the snow change. These changes result in alteration of the radar backscatter properties of the snow.

The snow liquid water content, m_v, the per cent of liquid water by volume present in the snow, has a dramatic effect on the electrical properties that make melt detectable by microwave sensors. Intrinsically, m_v is a function of depth. Here we consider the effect that m_v and other snow parameters have on the normalized backscatter, σ^o, observed by QuikSCAT and SeaWinds with the aid of a simple layered model that parameterizes the melt with depth.

When initially dry snow melts, the imaginary part of the effective dielectric constant ε'' increases very rapidly. As liquid water formation begins, ε'' increases sharply, changing by more than an order of magnitude (Ulaby *et al*. 1986). This drastic increase changes the backscattering and absorbing properties of the snow from a backscattering, weakly absorbing material to a weak backscattering, strongly absorbing material. The resulting backscatter of the wet snow drops considerably compared to the backscatter of dry snow. Thus, because of the electrical property changes, melting decreases the backscatter contribution from the melting snow, and attenuates the backscatter contribution of snow beneath.

The snow wetness and its effect on the backscatter depend on the concentration and depth of the melt. The effect of concentration and depth of melt can be addressed using a simple layered model (Ashcraft and Long 2006a). This model simplifies the effects of melt by dividing the backscatter contribution into a contribution from a wet snow layer of uniform properties on the surface, beneath which dry snow is found. Thus, the backscatter from melting snow can be described by

$$\sigma^o = \alpha^2 \sigma^o_{\text{dry}} + (1 - \alpha^2)\sigma^o_{\text{wet}}, \tag{1}$$

where $\alpha = e^{-\kappa_{e,\text{wet}} \sec\theta_w d}$, $\kappa_{e,\text{wet}}$ is the extinction coefficient of the snow when wet, d is the depth of the melt, θ_w is the transmission angle through the wet snow, σ^o_{wet} is the backscatter from the snow when entirely wet and σ^o_{dry} is the backscatter from the snow when completely dry. Subsurface scattering (which may be significant due to bulk ice formations such as ice lenses, glands and pipes) is included in the bulk scattering coefficient σ^o_{dry}, the backscatter that is observed when the snow is completely refrozen.

This two-layer model (illustrated in figure 1) is a very simple model of the snowpack in melt conditions. While the melt concentration in real snow is not uniform over the observation footprint, over the scale of the scatterometer resolution a uniform equivalent melt can be defined that results in the same net attenuation. The parameters of this model, σ^o_{dry}, σ^o_{wet} and α, vary spatially over the Greenland ice-sheet. When σ^o_{dry} and σ^o_{wet} are known, the backscatter can be used to infer the attenuation parameter α, which is a measure of the attenuation due to melt, and thus a measure of the melt severity, that is, how much liquid water is present.

Returning to equation (1), we solve for α^2,

$$\alpha^2 = \frac{\sigma^o - \sigma^o_{\text{wet}}}{\sigma^o_{\text{dry}} - \sigma^o_{\text{wet}}}. \tag{2}$$

Since $\alpha = e^{-\kappa_{e,\text{wet}} \sec\theta_w d}$, equation (2) simplifies to

$$\kappa_{e,\text{wet}} d = \frac{\cos\theta_w}{20 \log_{10} e} \left[\frac{\sigma^o - \sigma^o_{\text{wet}}}{\sigma^o_{\text{dry}} - \sigma^o_{\text{wet}}} \right]_{\text{dB}}, \tag{3}$$

which has units of neper (Np). Because of the difficulty of determining $\kappa_{e,\text{wet}}$, no attempt is made to infer the melt depth d. Instead, in this model we note that the parameter $\kappa_{e,\text{wet}} d$, captures all the parameters of the two-layer model that are affected by the severity of melt.

From equation (3) and noting that σ^o_{dry} is significantly larger than σ^o_{wet}, we can define a simple time-dependent MSI $\chi(t)$ as

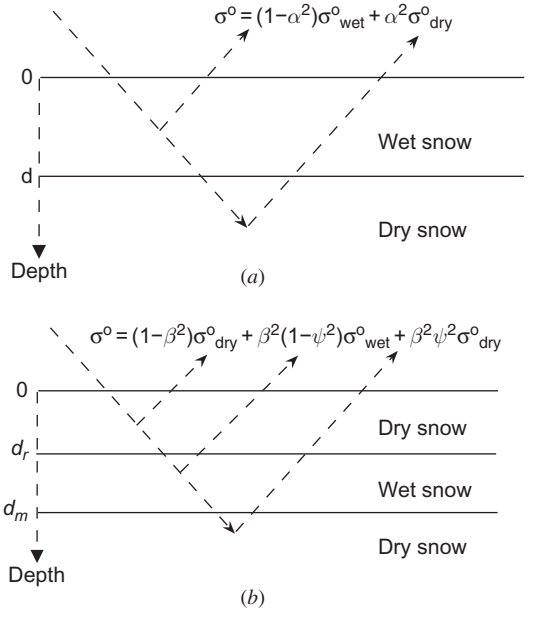

Figure 1. Diagrams of multi-layer backscatter models. (*a*) Two-layer model. (*b*) Three-layer model. Model parameters are described in the text.

$$\chi(t) = \frac{\cos\theta_w}{20\log_{10} e}\left(\sigma^o_{\mathrm{dry}} - \sigma^o(t)\right), \tag{4}$$

where σ^o_{dry} and $\sigma^o(t)$ are now expressed in dB. The MSI provides a useful measure of the time-varying amount of melt and corresponds to $\kappa_{e,\mathrm{wet}}d$ when the assumption that $\sigma^o_{\mathrm{wet}} = 0$ is made. Later, we introduce the integrated MSI as a measure of seasonal melt intensity.

As a measure for the amount of melt, the MSI is imperfect. First, noise corrupts σ^o and thus χ. Second, the model does not account for snow stratification, but lumps the backscatter contribution from all layers into a single parameter σ^o_{dry}. This parameter may vary during the course of a year because the stratified layers of snow are altered during the melt season when some layers are so completely changed that they disappear as melt and vapor transport occur. Such changing properties may therefore introduce a bias in the index. Third, not including σ^o_{wet} in the MSI results in a dependence on snow type and saturation during heavy melt. Nevertheless, the MSI is a good indicator of melt severity that can be derived from backscatter measurements without requiring *a priori* information about snow conditions. Future work incorporating *a priori* snow information is planned to enable liquid water formation inference from the MSI value.

2.2 *Layered refreeze model*

Measuring the refreeze process, like measuring the melt process, is complicated due to the gradual changes in the snow properties affecting backscatter; however, the measurement of the refreezing process is further complicated by the thermodynamic

conditions that drive the refreeze. For this reason, using the two-layer model may not accurately describe the changes in backscatter contribution during the refreeze process. In particular, melt, which is due to solar and atmospheric forces, proceeds from the surface downward while the propagation of refreeze may occur from beneath the wet layer upward as well as from the surface downward.

During melt, heat flows into the snow from the surface. This heat is drawn deeper into the snow-pack by conduction to the colder subsurface layers. During the refreeze process, heat continues to be drawn deeper into the snow-pack by conduction, refreezing the snow from beneath. At the surface however, the flow of heat varies: heat may continue to be delivered into the snow at a slower rate, or may be drawn out of the snow by convection and radiation. If heat is being drawn out of the snow at the surface during refreeze, a layer of refrozen snow forms at the surface. The presence of a frozen layer at the surface has a considerable effect on the backscatter. Thus, the two-layer model during refreeze may be inadequate. Accordingly, a three-layer model is proposed for refreeze.

A diagram of the proposed three-layer model is shown in figure 1. The three-layer model allows the refreeze of the centre layer to propagate both from the surface downward and from beneath the wet-snow layer upward. The existence of a subsurface wet snow layer is consistent with passive radiometer observations (Mätzler 1994), and SSM/I channel ratios (Ashcraft and Long 2005). Under this model, the equation for the total backscatter can be separated into contributions from each of the three layers. The total backscatter can be described by

$$\sigma^o = (1-\beta^2)\sigma^o_{\text{dry}} + \beta^2(1-\psi^2)\sigma^o_{\text{wet}} + \psi^2\beta^2\sigma^o_{\text{dry}}, \tag{5}$$

where $\beta = e^{-\kappa_{e,\text{dry}} \sec\theta_d d_r}$ and $\psi = e^{-\kappa_{e,\text{wet}} \sec\theta_w (d_m - d_r)}$. In these expressions $\kappa_{e,\text{dry}}$ is the extinction coefficient of dry snow, d_r is the depth of the top layer of refreeze and $d_m - d_r$ is the thickness of the remaining wet snow layer.

It is impossible to uniquely recover the depths d_m and d_r simultaneously for a single σ^o measurement; thus, additional information is needed about either d_m or d_r. Since refreeze follows melt, more is known about the melt depth d_m than d_r. Because the propagation of refreeze from beneath the partially melted layer is caused by a relatively constant flow of heat downward, one possible treatment is to assume d_m changes linearly with time. This, however, adds another unknown parameter to the model. A simpler approximation that does not require additional parameters is to assume that d_m is constant. When the melt depth is large, changes in d_m have relatively little impact on the backscatter due to the attenuation of the wet layer. Note, however, that this assumption requires that refreeze propagates from the surface downward – a good approximation given that this appears to be a dominant refreezing mechanism in the Greenland ice-sheet as shown later.

The equation for backscatter in the three-layer model using the assumption that $\sigma^o_{\text{wet}} = 0$ is

$$\sigma^o = \left[1 - \beta^2(1-\psi^2)\right]\sigma^o_{\text{dry}}. \tag{6}$$

Using $\chi = \kappa_{e,\text{wet}} d_m$, $\xi = \kappa_{e,\text{wet}} d_r$, $\gamma = \kappa_{e,\text{dry}}/\kappa_{e,\text{wet}}$ and $\sec\theta_d = \sec\theta_w = \nu$, we can write β and ψ as functions of χ, ξ, γ and ν:

$$\beta = e^{-\gamma \nu \xi}, \tag{7}$$

$$\psi = e^{-\nu(\chi - \xi)}, \tag{8}$$

where χ is the MSI estimated during the previous melt state, ξ is a parameter similar to χ – a theoretical measure of the thickness of frozen snow above the wet subsurface layer – while γ and ν are constants. The parameter ξ is referred to as the refreeze severity index (RSI).

Like the MSI, the RSI has limitations. Both β and ψ are dependent on ξ; thus, this index is not explicitly invertible. It is one-to-one, however, and can easily be inverted numerically using the well-known Newton–Raphson method, which is known to converge quadratically when it converges. Although a more sophisticated technique could be used, adequate results are obtained, and no convergence problems have been observed.

We note that the RSI depends on knowledge of γ and ν. While ν is practically constant regardless of the type of snow, γ depends on the snow parameters. Figure 2 shows the refreeze index ξ versus $\sigma^o - \sigma^o_{\text{dry}}$ for various initial values of χ_{melt}. As the initial melt increases, ξ becomes increasingly nonlinear, particularly for large χ_{melt} and small ξ where large changes in σ^o drive small changes in ξ. The degree of nonlinearity is largely dictated by the extinction ratio γ. For small γ, the nonlinear effect appears only for large χ_{melt}, and the onset of this nonlinear behaviour is less severe. Large γ causes the nonlinearity to be much more severe, and appears at smaller initial melt values. Since the extinction coefficients are dependent on the parameters of the snow, this model suffers from additional error where γ is different from the assumed value.

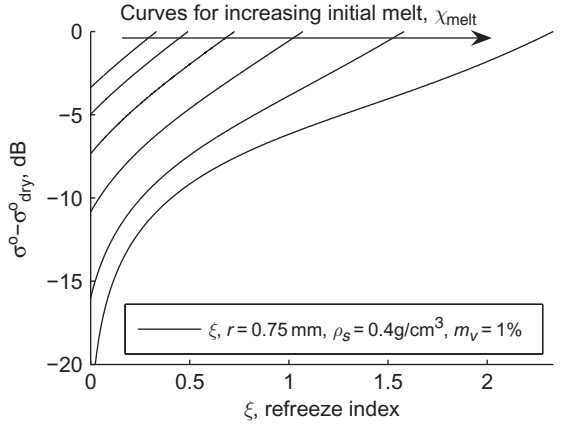

Figure 2. The relationship between RSI, ξ and $\sigma^o - \sigma^o_{\text{dry}}$ for various initial values of χ_{melt}. The dry snow has a grain size, $r = 0.75$ mm, density $\rho_s = 0.4$ g cm^{-3}, resulting in a relative permittivity of $\varepsilon_{r,\text{dry}} = 1.53$ and extinction coefficient of $\kappa_{e,\text{dry}} = 1.20$. The wet snow has the same grain size and density with moisture content, $m_v = 1\%$, resulting in $\varepsilon_{r,\text{wet}} = 1.57 - j3.35 \times 10^{-2}$ and $\kappa_{e,\text{wet}} = 12.12$. Permittivity is estimated using a modified Debye-like model (Ulaby *et al.* 1990). Scattering coefficients are estimated using a method involving spherical ice inclusions in an air–water background where permittivity is determined by the Polder–Van Santen mixing formula (Ulaby *et al.* 1990). Note that as the initial melt depth, χ_{melt}, increases, ξ becomes increasingly nonlinear.

Fortunately, despite the inconsistency of nonlinear effects in ξ across varying snow types, the RSI is not particularly sensitive to the exact snow parameters. Snow grain size has the largest effect, followed by moisture concentration and snow density, respectively. Since snow grain size is quite variable across the snow-pack, the exact response of ξ to refreeze suffers from modelling errors due to unmodelled variations. However, the qualitative behaviour between σ^o and ξ is similar regardless of the exact choice for γ. In warmer, more frequently melting regions the snow has generally larger grains, larger γ, and thus more nonlinearity in the refreeze index. In these regions the effective refreeze depth is thus likely to be overestimated. In drier, cooler regions, the grain size is expected to be generally smaller, causing the refreeze index to be underestimated. However, cooler regions are also less likely to experience severe melt and thus remain within the nearly linear regime of the response curves.

2.3 *Markov melt classification model*

The three-layer model provides a framework for selecting between two states for the ice-sheet: melt or refreeze. The ability to separate melt from refreeze is important to the study of many ice-sheet parameters including ablation, which occurs as liquid water leaves the ice-sheet by runoff, evaporation or sublimation, and other processes driven by the availability of liquid water near the surface.

Previous studies have focused on determining if the snow was dry or contained liquid water, based on changes in the radar backscatter. However, by following the change in backscatter with time, and assuming that the temporal resolution of the measurements is sufficiently high, distinguishing melt from refreeze becomes possible. To this end, a constrained one-step Markov chain model is proposed. The constrained model allows past state knowledge to influence the decision rule used in determining the current ice-state. Each state has its own decision rule for determining the next state. Clearly, refreeze cannot be considered unless melt has been previously detected.

For realistic detection and classification of the melt state, the thresholds need to be chosen within the limitations of the model and the sensor systems to reduce the classification error. Selection of the threshold is described in the following subsections.

2.3.1 Frozen state. In our Markov melt model there is only one possible transition from frozen state: frozen to melting. A threshold that is a function of σ^o allows the separation of the frozen state from the melt state. Let $S(t_n)$ represent the state of the ice at time t_n, that is

$$S(t_n) = \begin{cases} 0 & : \text{ frozen} \\ 1 & : \text{ melting} \\ 2 & : \text{ refreezing.} \end{cases} \tag{9}$$

The decision rule for determining the state at the next time step, t_{n+1}, is $S_i(t_{n+1})$, where $i = 0, 1, 2$ is the current state: frozen, melting and refreezing, respectively. The decision rule when the current state is frozen is

$$S_0(t_{n+1}) = \begin{cases} 0 & : \quad q(t) < q_0 \\ 1 & : \quad q(t) \geq q_0, \end{cases} \tag{10}$$

where $q(t)$ and q_0 are the metric and threshold, respectively, and which are defined in the following.

In the frozen state, the two-layer model is used. Melt detection is done using a modified form of the Q-α method developed by Ashcraft and Long (2006a). In this method, melt is detected by computing the scaled MSI, $q(t) = \sigma^o_{\text{dry}} - \sigma^o$. Values less than a threshold q_0 are declared melt. A melt classification threshold of $q_0 = 3$ dB corresponds to a depth of 2.4 cm for snow with a m_v of 1.0%, grain size of 0.75 mm, $\rho_s = 0.4\ \text{g cm}^{-3}$ (Ashcraft and Long 2006a). These snow properties are consistent with observations of Greenland snow (Benson 1962). While Ashcraft and Long (2006b) compensated for sastrugi-induced directional variation of σ^o, this is not done in this work.

2.3.2 Melt state. The melt state has two transitions: one to the refreeze state, and the other to the frozen state. While the transition directly from melt to frozen is not strictly necessary, the roughly eight hours of elapsed time between observations in the tandem data time series makes complete refreeze plausible for short melt events. The decision rule for the melt state is

$$S_1(t_{n+1}) = \begin{cases} 0 & : \quad q(t) < q_1 \\ 1 & : \quad r(t) \le r_0, q(t) \ge q_1 \\ 2 & : \quad r(t) > r_0, q(t) \ge q_1, \end{cases} \tag{11}$$

where $q(t)$ is as defined previously, q_1 is the threshold of this metric and $r(t)$ and r_0 are a metric and threshold, respectively, used to distinguish between melt and refreeze. Since the transition from melt to frozen is a special case of the refreeze to frozen transition, q_1 is determined later where the transition to frozen is covered in greater detail.

The difference between the melt and refreeze states is defined by the change of liquid water in the snow. Melt is characterized by increasing liquid water, while refreeze is characterized by decreasing liquid. Since the attenuation in σ^o is related to the amount of liquid water in the snow, the sign of $\frac{\partial \sigma^\circ}{\partial t}$ can be used to determine if melt or refreeze is occurring. Hence, temporal changes in σ^o determine $r(t)$ and r_0.

Using a one-step Markov model $\frac{\partial \sigma^\circ}{\partial t}$ is approximated by $r(t_n) = \sigma^o(t_n) - \sigma^o(t_{n-1})$, which is used as the melt-to-refreeze metric. Without noise, a simple threshold, $r_0 = 0$, would properly distinguish between these two states according to their definitions. In practice, however, noise is a concern. As seen by the response curves of the RSI shown in figure 2, the formation of frozen snow at the surface during refreeze causes a rapid increase in backscatter. Since refreeze is more readily apparent than continued melt, setting $r_0 = k$ where k is some positive constant, shifts the detection threshold to increase the probability that continued melt is detected compared to refreeze. Thus, k is used to balance the difference in sensitivity between refreeze and continued melt. We let $k = 0.5$ dB, which appears to be an acceptable threshold based on the simulation experiments described in §3.1.

2.3.3 Refreeze state. From the refreeze state, the possible transitions can be to a state of frozen, melting or continued refreeze. The decision rule is

$$S_2(t_{n+1}) = \begin{cases} 0 & : \quad q(t) < q_1 \\ 1 & : \quad r(t) \le r_0, q(t) \ge q_1 \\ 2 & : \quad r(t) > r_0, q(t) \ge q_1. \end{cases} \tag{12}$$

A separate threshold q_1 for the water content metric is used for the transition back to the frozen state. This threshold differs from the melt threshold to enable adjustment of decision boundaries and avoid limiting the maximum observable ξ, see figure 2. We select $q_1 = 1$ dB to ensure that most of the refreeze process is accounted for, while maintaining the threshold far enough away from σ^o_{dry} to minimize misclassification due to noise. This threshold value ensures that at least 60% of the refreezing process is observable under light initial melting conditions, and more than 90% of the refreezing process is observable under moderate to heavy melt.

The decision rules governing all state transitions are summarized in table 1.

2.4 *Geophysical simulation model*

In order to evaluate the expected backscatter temporal variation and select and validate classification thresholds a simple geophysical snow-ice model is used to simulate backscatter measurements. Ideally, a sophisticated snow model such as the well-known SNTHERM (SNow THERmal Model; Jordan 1992) would be used, but SNTHERM requires more detailed information about the snow than is available in our application. Instead, a much simplified multi-layer one-dimensional geophysical snow-ice model is employed that considers thermodynamic properties, water percolation, and, to a limited extent, the metamorphism and settling of the snow-pack (Hicks 2006). We note that our results are not particularly sensitive to the details of the snow simulation and that the simulation model described in this section is not part of the indices computation described earlier, other than for helping select threshold value.

A one-dimensional equivalent model is employed in this application because the area of a single pixel is very large compared to the vertical extent of the model. The layers of the model, which are control volumes with constant properties, are illustrated in figure 3. The physical properties of the control volume layers obey the laws of conservation of energy and mass, which govern the temperature and the formation and flow of liquid water. The model simulates snow–ice evolution over several days. For each temporal increment, the model algorithm has several steps. A block diagram of the algorithm is shown in figure 3. Each iteration consists of

(i) thermodynamic diffusion governed by the heat diffusion equation and driven by a surface heat source,
(ii) melt determined by the energy required to heat each control layer above 0°C,
(iii) settling,
(iv) percolation,

Table 1. Decision rules for state change, from current state $S(t_n)$ to next state $S(t_{n+1})$, written in terms of $\sigma^o(t_n)$ and $\sigma^o(t_{n+1})$.

	$S(t_n)$	
$S(t_{n+1})$	Frozen	Melting or refreezing
Frozen	$\sigma^o(t_{n+1}) > \sigma^o_{\text{dry}} - 3\text{dB}$	$\sigma^o(t_{n+1}) > \sigma^o_{\text{dry}} - 1\text{dB}$
Melting	$\sigma^o(t_{n+1}) \leq \sigma^o_{\text{dry}} - 3\text{dB}$	$\sigma^o(t_{n+1}) \leq \sigma^o_{\text{dry}} - 1\text{dB}$ $\sigma^o(t_{n+1}) < \sigma^o(t_n) + 0.5\text{dB}$
Refreezing	—	$\sigma^o(t_{n+1}) \leq \sigma^o_{\text{dry}} - 1\text{dB}$ $\sigma^o(t_{n+1}) \geq \sigma^o(t_n) + 0.5\text{dB}$

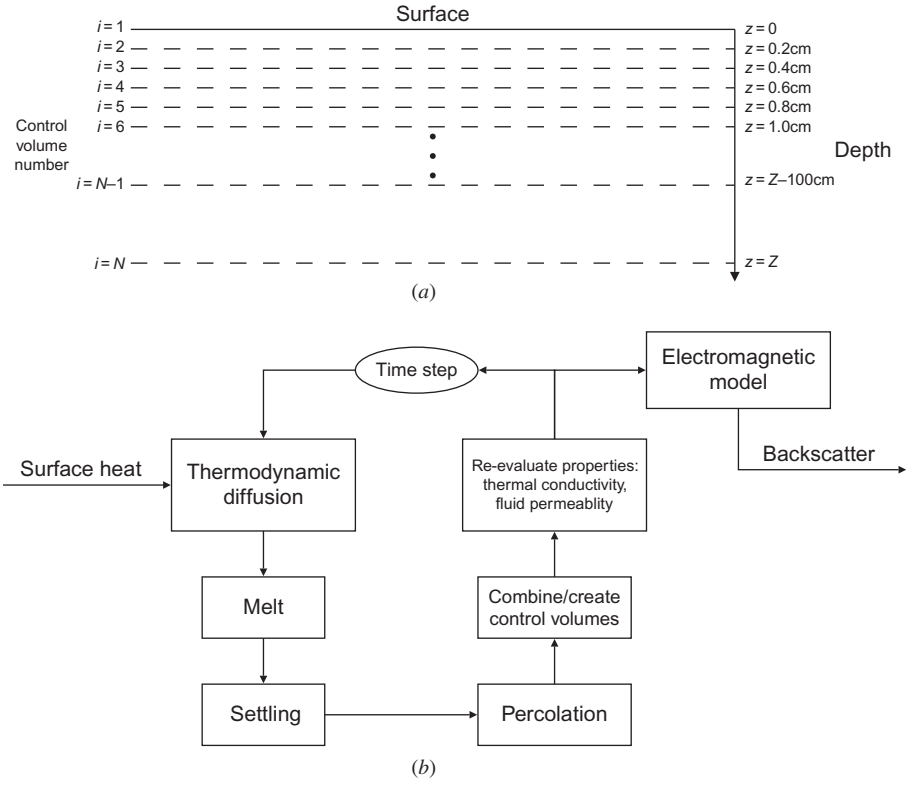

Figure 3. Illustrative diagrams for the one-dimensional geophysical–electromagnetic simulation model. (*a*) Model layers showing the control volumes. (*b*) Algorithm flow.

(v) combining small control volumes, and creating new volume elements to maintain model depth,
(vi) re-evaluation of snow properties such as thermal conductivity, fluid permeability, etc. and
(vii) application of the electromagnetic model to infer the backscatter.

The thermodynamic portion of the model is governed by the heat diffusion equation

$$\frac{\partial T(z,t)}{\partial t} = -\frac{1}{\rho(z)C_p}\frac{\partial}{\partial z}\left(\lambda(z)\frac{\partial T(z,t)}{\partial z}\right), \tag{13}$$

where $T(z, t)$ is the temperature at depth z and time t, $C_p = 0.21$ J g^{-1} K^{-1} is the specific heat of snow and $\lambda(z)$, $\rho(z)$ are, respectively, the thermal conductivity of snow and the snow density at depth z. This equation is discretized and is solved iteratively using the widely known Crank–Nicholson implicit method. A Dirichlet boundary is used on the bottom layer, which holds the temperature at that node constant. A time-varying heat source is applied at the surface. This heat source is a combination of the net effective heat transport to and from the atmosphere that includes convection, radiation and sensible and latent heat flux. While this is an oversimplification – significant heat leaves

by vapor transport and forced convection from beneath the surface – the details of the transport have little effect on backscatter so long as all the heat is accounted for.

To determine melt and refreeze, potential temperatures greater than 0°C are reduced to 0°C, and the excess heat is used to convert the snow to liquid water. The temperature in excess of 0°C has energy density $Q_e = \rho C_P(T - T_{0C})$, which causes melting and results in an increase in the fraction of liquid water. The density of newly melted liquid water is $M_l = Q_e/L_f$ where L_f is the latent heat of fusion (334 J g^{-1}). For refreeze in layers with liquid water, where the heat diffusion computes temperatures below 0°C, the temperature is set to zero and the heat lost is converted to frozen water until the layers' water is completely refrozen.

Percolation is evaluated by assuming that percolation does not occur until a minimum fraction of the snow has melted (Colbeck 1979). Above this saturation concentration, water begins to percolate downward. Percolation obeys conservation of mass, requiring that

$$\frac{\partial(\rho \, \mathrm{d}V \, m_v)}{\partial t} = -[U_l]_i^{i+1} + M_{li}, \tag{14}$$

where $-[U_l]_i^{i+1}$ is the vertical water flux evaluated at the control volume surfaces, M_{li} is the liquid-to-ice flux, with

$$U_l = \frac{\rho_w}{\mu_w} g K_{\max} \left[\frac{s - s_r}{1 - s_r}\right]^3, \tag{15}$$

where $\rho_w = 1.0$ g cm^{-3} is the density of pure water, $\mu_w = 10^{-6}$ m^2 s^{-1} is the kinematic viscosity of water, g is the gravity acceleration, $K_{\max} = 0.077d^2 \exp(-7.8\rho_s/\rho_w)$ is the intrinsic snow permeability, d is the grain size, $s = v_l/(1 - v_s)$ is the water saturation, $v_l = \rho_l/\rho_w$ is the specific volume of liquid water, $v_s = \rho_s/\rho_i$ is the specific volume of ice, $\rho_i = 0.917$ g cm^{-3} is the density of pure ice, and s_r is the residual water saturation (Colbeck 1979).

Because of the large scale of the scatterometer measurement footprint (> 6 km), a statistical equivalent bulk model is assumed; thus, the percolation and resulting effect on σ^o is considered only in the average sense. For simplicity the downward flow of water is assumed to be spatially uniform, which for the purpose of bulk modelling is considered adequate. It is noted, however, that the actual flow pattern is quite irregular, forming fingers and channels which cause the leading edge of melt to disperse. The density variations in a realistic snow-pack may also have horizontal flow. However, a model that handles this behaviour is significantly more complicated and requires more *a priori* information than is available for this study; thus, vertical dispersion and horizontal flow are ignored.

The residual water saturation, s_r, is a critical parameter that determines the minimum water saturation that must be present for percolation to occur. Different values are found throughout the literature, generally between 0.02 and 0.1 (Rowe *et al*. 1995, Gallée and Duynkerke 1997, Lefebre *et al*. 2003). Our model uses $s_r = 0.065$, though other values are considered in the simulation shown below. This value of s_r results in a m_v between 3% and 5% for typical melt conditions and firn densities. We note that the residual water saturation, and thereby the liquid water content

of the snow, has a profound effect on the absorption coefficient, κ_a, during melting conditions. The effect of the s_r parameter on the backscatter is discussed further in §2.4.2.

A very simple algorithm is used for settling, densification and snow metamorphism (Hicks 2006). When a portion of the snow melts in a control volume, the layer thickness is decreased so the snow fraction density stays the same. Thus, melting causes the snow to settle. Densification occurs as the melt refreezes, where the liquid fraction is added to the snow fraction. This is the only mechanism considered for densification. In the simulation, the grain size is held constant due to the complexity of current state-of-the-art grain models, for example, SNTHERM. This is recognized as a limitation of our simplistic model. However, we note that while grain size has an effect on the backscatter, grain size modification only adjusts the backscatter by a few tenths of a dB.

Layers that become too thin due to melt are combined with adjacent layers. The three nearest layers, including the thin layer being deleted, are combined into two equal layers, each taking half of the thin layer. The three to two combination minimizes discontinuities in the backscatter compared to merely deleting the layer. Layers near the surface – within the top 30 cm – are initially 0.2 cm thick. When a layer becomes thinner than 0.1 cm, layers are combined. The near-surface layers are set much thinner than typically used in one-dimensional snow models (Rowe *et al*. 1995, Lefebre *et al*. 2003) since σ^o is very sensitive to the electrical properties in the top several centimetres of wet snow. In the model, layers deeper than 30 cm increase in thickness at each step, see figure 3. The bottom-most layer is 1 m thick. When the model depth decreases to 0.5 m, a new 1 m layer is added to the bottom.

2.4.1 Model simulation initialization. To initialize the model, an initial snow density $\rho_s(z)$ at the surface of 0.36 g cm^{-3} is assumed with an increasing density with depth following Benson (1962). A quadratic regression model for λ (Sturm 1997) is used where $\lambda = 0.138 - 1.010\rho_s + 3.233\rho_s^2$ W m^{-1} K^{-1}. The snow temperature profile is initialized according to

$$T(z,0) = T_\infty + (T_\infty - T')\sqrt{\frac{z+z'}{Z+z'}}, \tag{16}$$

where $T_\infty = -35°$C is the temperature at ultimate model depth $Z = 20$ m, T' is chosen so the top layer is 0°C, and m is used to insure that the gradient $\frac{\partial T}{\partial z}$ is bounded at $z = 0$ and the solution remains smooth for $t > 0$. All model parameters are constant across each control volume.

The thermal model requires a heat input at the surface to drive the melting process. We assume a single uniform heat source applied at the upper surface of the model that represents the net heat flux exchanged with the atmosphere (e.g. solar, IR, sensible and latent heat flux, etc.). In the experiments that follow, two heat flux cases are considered: a constant heat flux and an offset sinusoidally varying heat flux. The sinusoidally varying heat flux is $\Phi_Q = 0.75 + 5\sin\frac{\pi}{7}t + 7\sin 2\pi t$, W m^{-2}, where t is in days. In this expression the offset maintains the average temperature of the snow near the surface. The two sinusoids represent a high-amplitude diurnal signal and a medium-amplitude 14-day-signal which simulates variations in heat flux due to a large scale weather pattern. The model thus represents a 14-day-long period with diurnal variation with a major storm front similar to that seen in tandem QuikSCAT–SeaWinds and AWS

data from JD 152 to JD 170, 2003 at the ETH Swiss Camp, shown later in figures 7 and 9.

2.4.2 Electromagnetic model. A simplistic electromagnetic backscatter model is employed to compute backscatter from the snow conditions. While the geophysical–electromagnetic model used is very simple, it produces reasonable results suitable for this study. The experiments explained in the next section yield good agreement with tandem SeaWinds backscatter measurements taken at the ETH Swiss Camp shown later in figures 7 and 9 and seen in σ^o images across the ice-sheet. While the results are inexact due to the simplifications employed, the qualitative behaviour of the model follows the observed measurements quite well.

The electromagnetic backscatter model uses the snow state from the geophysical model to estimate the vertically-polarized normalized radar cross-section of the snow viewed at or near the Brewster angle. At this angle, surface and inter-layer reflections are negligible. The model estimates the backscatter using a general equation for volume backscatter,

$$\sigma^o = \int_0^\infty \gamma(z) e^{-2\tau(0,z)} \sec\theta(z) \mathrm{d}z, \tag{17}$$

where $\gamma(z)$ is the volume contribution and $e^{-2\tau(0,z)}$ is the attenuation. Since the magnitude of the permeability is relatively constant with depth, the term $\sec\theta(z) = \sec\theta \approx 1.1656$ can be moved out of the integral. Attenuation is estimated using a radiative transfer model where the optical depth of the snow-pack is

$$\tau(0,z) = \sec(\theta) \int_0^z \kappa_e(z') \mathrm{d}z'. \tag{18}$$

The extinction coefficient, κ_e, is a function of the physical parameters of the snow. The extinction coefficient is the sum of the scattering coefficient and the absorption coefficient, $\kappa_e = \kappa_s + \kappa_a$. Absorption coefficients are estimated using a modified Debye-like model (Ulaby *et al*. 1990) to obtain the complex permittivity of the snow, ε_r, with the absorption related to permittivity by

$$\kappa_a = 2\frac{2\pi f}{c} \Im\{\sqrt{\varepsilon_r}\}, \tag{19}$$

where f is the frequency, c the speed of light in a vacuum and $\Im\{\cdot\}$ denotes the imaginary part. The scattering coefficient is found by modelling the snow grains using independent Mie-scattering of spherical ice inclusions in an air background. While better scattering models that incorporate the interaction of scattered waves between scatterers exist, these models require additional information such as surface correlation length, which is unknown at most locations. The scattering coefficient is assumed constant with water content. The snow density ρ_s, the grain size r and the liquid concentration m_v are inputs to the model. Once the extinction coefficient is determined for each control volume, the integral of equation (18) is estimated using the extended Simpson's rule for each depth. Once τ is determined, the attenuation can be computed.

The volume backscatter contribution, $\gamma(z)$, in equation (17) depends on the snow state. For dry snow, the volume contribution is assumed to be proportional to the

scattering coefficient, κ_s. Adding liquid greatly increases absorption while only slightly affecting scattering. Thus, for the sake of simplicity, wet snow volume backscatter is assumed independent of water content. Here, we can relax our earlier assumption that $\sigma^o_{\text{wet}} = 0$ since the EM scattering model can directly compute the wet snow backscatter.

3. Results

In this section, the melt model described in §2.1 is combined with the geophysical–electromagnetic model to infer snow conditions in Greenland at selected sites. First, simulation experiments are conducted to compare the behaviour of the model compared to actual observations. Then, AWS data are used to validate the combined model at selected sites. Following the validation, the melt modeling method is applied to the entire ice-sheet. The ice-sheet melt estimates are then analysed.

3.1 *Simulation*

To evaluate the effectiveness of the new melt model, two simulation experiments are performed. The goal of the first experiment is to test the assumption in §2 that the melt depth, d_m, during the refreeze has only a relatively small effect on the backscatter, and thus that χ can be assumed to be constant during refreeze. The second experiment is conducted to illustrate how MS and RSI follow the melt through a simulated melt event in the percolation zone in Greenland. This result is compared to actual data in a succeeding section.

To conduct the first experiment, a constant heat flux of 5 W m^{-2} into the surface is imposed on the model with initial parameters stated in §2.4.1. The heat is allowed to penetrate the surface for 6 days, causing melt and percolation to occur. The depth of this melt depends on the residual water saturation, s_r, which determines how concentrated the water is in the wet snow layer. To evaluate the effect that s_r has on the backscatter and the time to refreeze, two values are considered, $s_r = 6.5\%$ and 3%. After applying the constant 5 W m^{-2} heat flux to the surface of the modelled snow for six days, the heat flux is changed to 0 W m^{-2} and a day is allowed to permit the percolation process to complete before backscatter measurement begins. Heat flux at the surface remains at 0 W m^{-2} for the duration of the backscatter measurements. At a heat flux of $\Phi_Q = 0$ W m^{-2}, the refreezing of the wet snow propagates from beneath the wet snow layer upward, with no refreeze occurring at the surface.

Figure 4 shows the outcome of the first experiment. The integrated liquid water beneath the surface at $t = 0$ is 0.49 cm w.e. Note that the water in the snow is modest, resulting in melt depths of 23.7 and 12.2 cm for $s_r = 0.03$ and $s_r = 0.065$, respectively, yet it takes 8–12 days for a measurable change in backscatter to occur when refreeze is propagating only from beneath the wet snow. Since the time to refreeze observed in actual backscatter measurements of Greenland are much shorter than this, we conclude that most of the refreeze must be originating at, and propagating from, the surface. This validates the assumption that χ is essentially constant during refreeze.

In this simulation, the temperature profile and the melt depth and mass are chosen to be consistent with expected conditions in the percolation zone, where melt is moderate. The temperature gradient in the wet snow zone is considerably more shallow. At the location of the ETH Swiss Camp where the AWS data is taken, the temperature below 10 m is approximately constant at −8.5°C (Greuell and Konzelmann 1994),

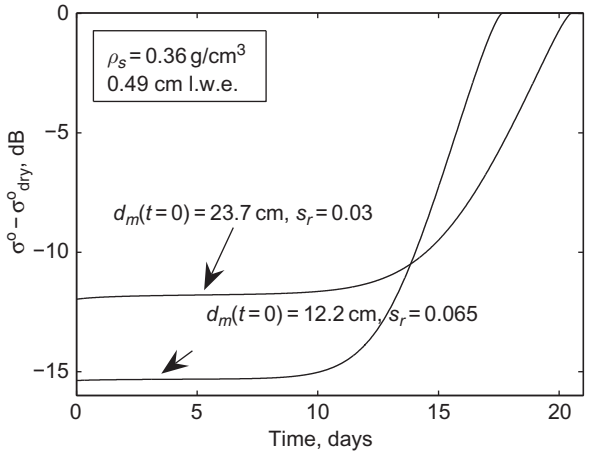

Figure 4. Outcome of the first experiment. The heat input at the surface is held at zero, while refreeze of the 4.90 km m^{-2} of liquid water is refrozen by heat transfer deeper into the snow. See text.

producing a temperature gradient much more shallow than the one used in the experiment. Moreover, the depth and quantity of melted water in this zone is much greater. Were this experiment repeated with melt and temperatures more consistent with those of the ETH Camp, the time elapsed before a notable change in backscatter would be considerably longer. Since this is not observed in σ^o data, the surface refreeze propagation must dominate. A second observation made during the first experiment is that σ^o, and thereby χ, saturates at relatively small melt depths when the melt concentration is held constant.

The second experiment attempts to simulate a melt event using a realistic heat input with diurnal variations. The heat input used is the offset sinusoidally varying heat flux described in §2.4.1. The residual water content is set to $s_r = 0.065$. Figure 5 shows the outcome of this experiment.

Several insights are gained from the second experiment. First, note that σ^o saturates during the day when the melt is at its peak during days 3–6. However, the backscatter still varies from day to night during these days, despite the fact that the surface never

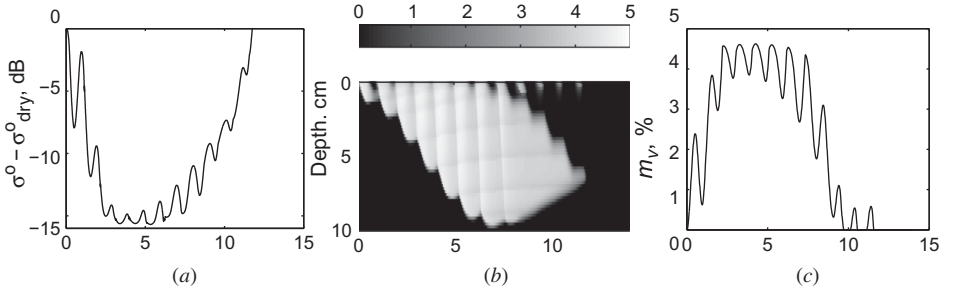

Figure 5. Results of model simulation experiment 2. (*a*) Backscatter versus time in days. (*b*) Depth and melt concentration versus time. (*c*) Mean melt concentration of the top 2.5 cm versus time.

completely refreezes. Second, note that σ^o closely follows changes in m_v in the top several centimetres of melt. Thus, for light melt, backscatter closely follows the melt depth; but for moderate-to-heavy melt, backscatter follows liquid concentration near the surface.

Because of the σ^o behaviour during melting conditions, the MSI follows the attenuation due to increasing melt depth for light melt, while for heavier melt it more closely follows σ^o_{wet}, which is a function of m_v and not the melt depth. As a result, the MSI follows the melt severity, though with decreasing sensitivity as the melt becomes more severe. Note that σ^o is very sensitive to refreeze, even for very thin surface refreeze layers.

To illustrate how the MSI and RSI are expected to appear in the tandem QuikSCAT and SeaWinds dataset, σ^o is sampled three times a day, corresponding to the tandem observation sample times, and the new melt detection and melt severity estimation technique is applied to the simulated backscatter data. Figure 6 shows the MSI, χ, and RSI, ξ, applied to the simulated backscatter. As this figure shows, χ increases as the snow pack melts, but saturates. As χ saturates, it follows the melt concentration in the top several centimetres, indicating that the MSI is following changes in σ^o_{wet}. Note also that the difference between the peak melt and peak refreeze for each day is well correlated to the thickness of the wet snow layer.

3.2 *ETH Camp AWS comparison*

To validate the new model-based melt detection method, the backscatter and resulting melt estimates are compared to data from an AWS located at the ETH Swiss Camp in Western Greenland. This station is situated in the wet snow zone of the ice-sheet and is characterized by frequent melt – ideal for the verification of the new melt model.

Figure 7 compares the tandem SeaWinds σ^o time series, the Swiss Camp AWS air temperatures, and a measure of the diurnal cycle magnitude. The diurnal cycle magnitude is evaluated using a simplistic matched filter. Match-filtering essentially measures the correlation between a signal and a reference. In this case, the reference is a sinusoid with a period of one day. This enables the measurement of both the magnitude and phase of the diurnal cycle. Backscatter that varies daily has high correlation with the sinusoidal matched filter and thus the filter output has a high output amplitude. To allow for fast transients from melt to refreeze, a short three tap filter $h[n]$ is used,

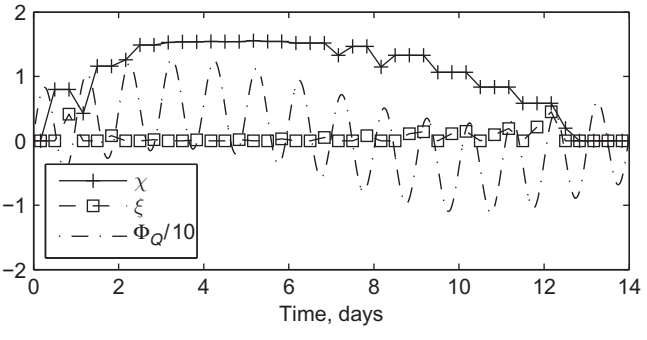

Figure 6. The MSI, χ, and RSI, ξ, for experiment 2 with $Z = 20$ m. The heat flux, Φ_Q, is scaled for clarity.

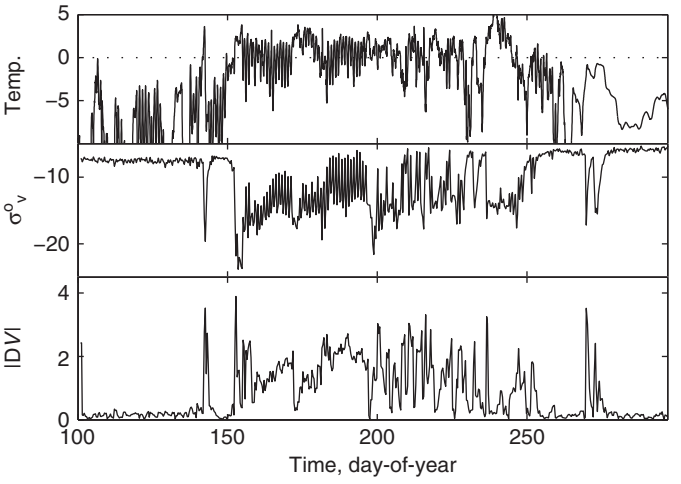

Figure 7. Top to bottom: AWS air temperature, σ^o, and the diurnal cycle amplitude, $|DV|$, measured by a three tap complex exponential filter. Located at Swiss Camp AWS, 69.57 N 49.30 W.

$$h[n] = \frac{1}{N} e^{-j\frac{2\pi}{3}n}, \tag{20}$$

where N is 3 and $n = [-1, 0, 1]$. The filter has a tendency to smear the sharp transitions but effectively captures the transient behaviour of the cycle variation. The filter output is the diurnal variation (DV),

$$DV[n] = h[n] * \sigma^o[n], \tag{21}$$

where * denotes convolution.

Several interesting features are seen in figure 7. First, the diurnal variation in σ^o can be considerable; note the high consistent diurnal cycle for JD 153 until JD 200. Good correlation is seen between the diurnal cycle of air temperatures near the 0°C isotherm and σ^o. It is also observed that the amplitude of the diurnal cycle in both air temperature and σ^o becomes more sporadic after JD 200, and is much smaller from JD 220 on. Note that the heat wave beginning JD 236 is characterized by low diurnal variation. Low diurnal variation is also observed during several other periods of low σ^o, for example, JD 154, 178 and 198. A scatter-plot of σ^o and $|DV|$ is shown in figure 8. We note that a wide range of DV values is present during intense melt when σ^o is very low. The DV spread is generally low when melt is not present.

Figure 9 presents a closer look at the time series in figure 7 from JD 145 to JD 168. A period of low backscatter and diurnal cycling is observed in this short time series. At the start of the time series when the snow-pack is frozen, the diurnal variation in σ^o is small while the value of σ^o is high. As the temperature climbs and remains consistently above zero, σ^o drops and remains low, with very little diurnal variation. As temperatures begin cycling above and below the 0°C isotherm, the daily mean of σ^o rises slightly, and a large diurnal cycle in σ^o is observed. During the time period from JD 163 to JD 166 the average air temperature drops and the portion of the day above

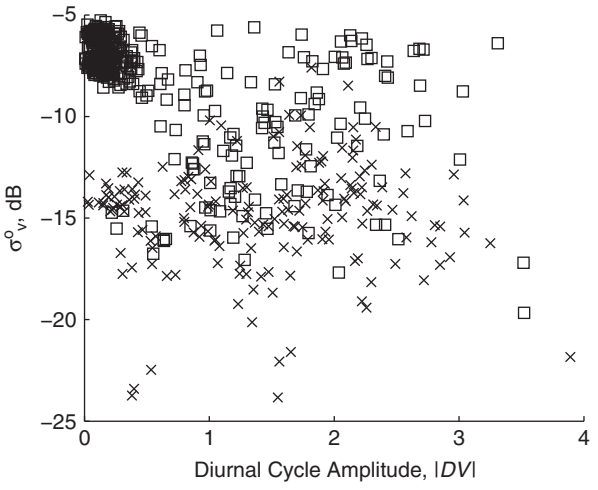

Figure 8. Scatter plot of σ^o versus diurnal cycle amplitude $|DV|$, as measured by a three tap complex exponential matched filter. The squares indicate when the surrounding air temperature is less than 0°C, while the ×'s show when the air temperature is greater than 0°C. Data is taken from the location of Swiss Camp AWS, 69.57 N 49.30 W.

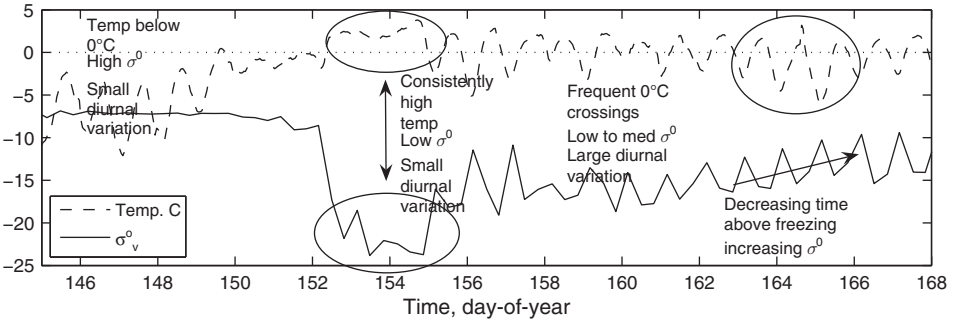

Figure 9. AWS Temp and σ^o time series for JD 145 to JD 168, 2003 at Swiss Camp AWS, 69.57 N 49.30 W.

0°C decreases. During this period the average σ^o increases, while maintaining a strong diurnal cycle. The σ^o peaks during this time period remain well below their winter values, suggesting that subsurface water is persistent. Such behaviour gives credence to the use of the three-layer model.

The strong diurnal variation of σ^o occurs when the diurnal variation of solar radiation is large, suggesting that melt during this period of time is driven primarily by solar heating. However, late season melt appears to be driven primarily by warm air masses, explaining the resulting decrease in diurnal cycle amplitude. The air temperature during the late season also appears to vary more slowly, suggesting perhaps, an increase in cloud cover insulating the ground from space.

Since melt is observed in many instances where the diurnal cycle amplitude is small in both figures 7 and 8, it appears that the diurnal cycle amplitude alone is insufficient for identifying melt. This result may, in part, explain some of the performance issues related to previous work (Nghiem *et al*. 2001). We postulate that strong melt events,

especially melt created by latent and specific heat input by convection from warm air masses, can continue during the night hours when solar radiation is negligible.

Figure 10 shows the MSI (χ) and RSI (ξ) at the ETH Swiss Camp location, with the air temperature provided for reference. The behaviour of the MSI and RSI correlates well with the temperature at this location. Because the new method of melt detection distinguishes separate melt events delimited by samples where the ice is frozen, a more detailed analysis of the behaviour of individual melt events is possible. To do this we define related indices such as the integrated melt severity index (IMSI) I_χ,

$$I_\chi = \sum_{k=1}^{N(t)} \chi_k \Delta t, \tag{22}$$

where $N(t)$ is the number of samples where melt is detected and $\Delta t = 8$ hours. The IMSI is useful for looking at seasonal melt strength. The difference between the MSI and RSI, referred to as the melt envelope (ME) $\psi = \chi - \xi$, provides an indication of the thickness of wet snow, especially the daily minimum ME, defined as

$$\psi_j^d = \min_{i=\{1,2,3\}} (\chi_{j,i} - \xi_{j,i}), \tag{23}$$

where j is the day of the year, and i is the ith sample of the day. The integrated melt envelope (IME) $I_{\chi-\xi}$ is defined as

$$I_{\chi-\xi} = \sum_{k=1}^{M(t)} (\chi_k - \xi_k) \Delta t, \tag{24}$$

where $M(t)$ is the number of samples where liquid water is present. Since the amount of liquid water – and its proximity to the surface – drives vapour transport, grain

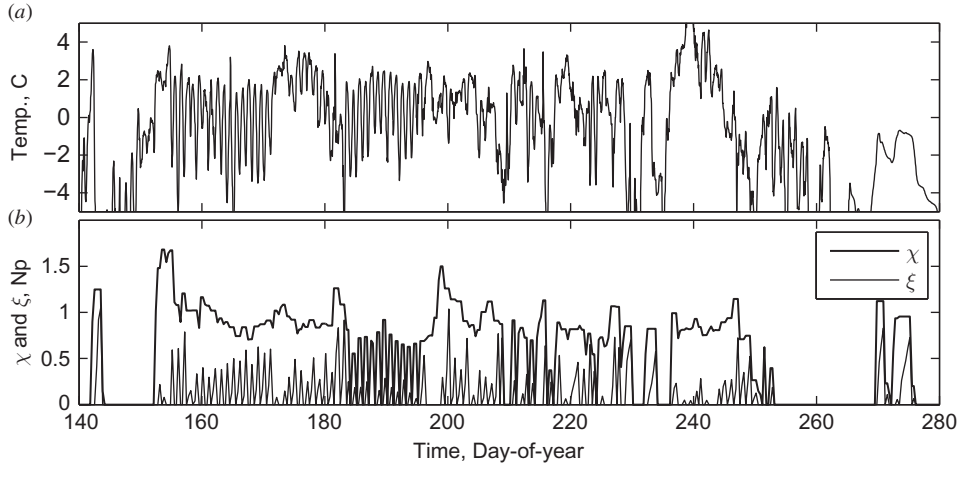

Figure 10. Comparison of MSI (χ), RSI (ξ) and AWS data. (*a*) AWS air temperature. (*b*) Backscatter-derived χ (thick line) and ξ (thin line). Data located at Swiss Camp AWS, 69.57 N 49.30 W.

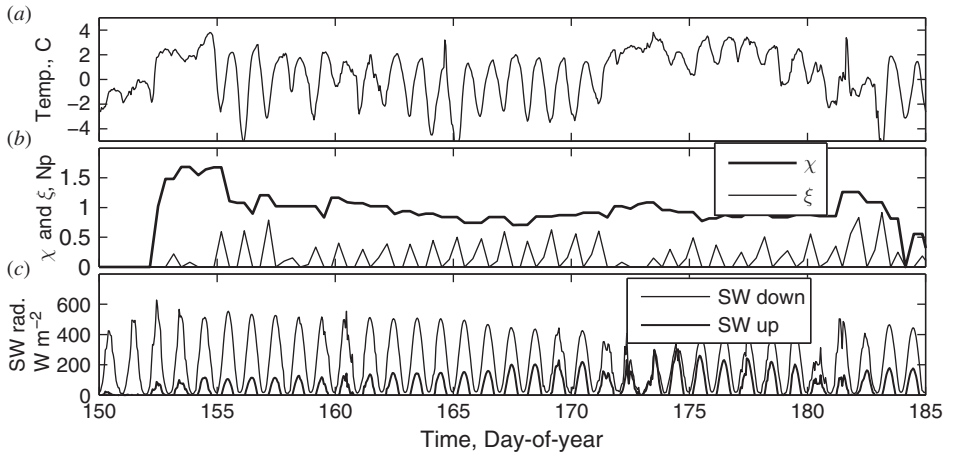

Figure 11. Expanded time series of MSI (χ), RSI (ξ) and AWS data during the longest melt event of 2003 at Swiss Camp AWS, 69.57 N 49.30 W. (*a*) AWS air temperature. (*b*) χ and ξ. (*c*) Upwelling and downwelling shortwave (SW) radiation.

growth, and other parameters that affect mass balance, the ME and related indices may prove useful. Table 2 summarizes a number of statistics and indices derived from backscatter at the ETH Camp.

The first and longest melt event during the 2003 melt season at the ETH Camp (JD 152–183) shows some interesting features and is helpful in illustrating the effectiveness of the MSI and RSI. The MSI, RSI, air temperature and up- and down-welling shortwave radiation (SW) are shown in figure 11. The beginning of the melt event on day JD 152, as identified by the Markov melt detector, is consistent with a peak in the net SW radiation, and a rise in air temperature above the 0°C isotherm. The beginning of melt is followed by several days (JD 152–154) where the air temperature remains above 0°C. The MSI and RSI correspondingly show heavy melt and little refreeze during this time period. During the mornings of JD 155–157, the air temperature drops well below 0°C, which should result in surface refreeze; the drop in MSI and strong cycling in the RSI clearly shows this trend. In the mornings between JD 157 and 158, and again between JD 159 and 160, the temperature drops below 0°C only for a short time. The RSI during these mornings is notably less than mornings before and after, mimicking the air temperature. A trend of dropping temperature and net SW radiation is seen during JD 160–165; the MSI and RSI capture this behaviour as MSI gradually decreases and RSI increases. Similar to JD 152–154, the temperature rises above 0°C during JD 172–175, though the net SW radiation is fairly low. During this time period, a constant melt is recorded by the MSI and RSI, though not nearly as strong as during JD 152–154, as expected by the high air temperature and low SW radiation. Days 175–180 show air temperatures constantly above 0°C; however, the RSI continues to show significant refreeze during this time. The net SW radiation during this time period is low, creating a net loss in total radiation, and leading to refreeze in the mornings despite higher air temperatures.

The analysis of the longest melt event at the ETH/CU Swiss Camp shows that the MSI and RSI reasonably follow the behaviour expected from air temperature and SW radiation data. We note that while these indices behave as expected, they do not

Table 2. 2003 melt statistics for the ETH/CU Swiss Camp AWS located at 69.57 N 49.30 W.

Statistic	Value	Description
T_b	142.1775	Beginning time of first melt, decimal JD
T_e	275.8400	Ending time of last melt event, decimal JD
T_{length}	133.6625	Melt season length, days
T_M	1202.6	Total time melting, h
T_L	2307.8	Total time wet snow is present, h
$t_{l,\text{longest}}$	760.2	Longest melt event, h
$\bar{t}_l$	85.4753	Mean melt event length, h
median(t_l)	16.4167	Median melt event length, h
std t_l	183.676	Standard deviation of melt event length, h
N_l	27	Number of melt events
max χ	1.6821	Maximum melt severity, Np
$\bar{\chi}_{\text{melt}}$	0.8474	Mean melt severity during melt, Np
$I_{\chi_{\text{melt}}}$	1020.3	Integrated melt severity, Np h
$I_{\chi-\xi}$	1652.0	Integrated melt envelope, Np h

directly translate into physical melt quantities. Nevertheless, their behaviour suggests that they may be a useful tool in deriving quantitative data at some point in the future. Particularly, improvements in surface property inversion techniques (Flach *et al.* 2005) may provide much needed *a priori* information, making the direct inference of melt quantities possible. It is hoped that the estimates provided by χ and ξ may be useful as model inputs from which physical melt estimates may be obtained.

3.3 *Ice-sheet melt estimation*

Having considered application of the new method to a single location, the new melt detection model is used to obtain a melt estimate over a larger area. The results are limited to only glaciated regions of Greenland, as indicated in figure 12. In this analysis, σ^o_{dry} is determined from tandem SeaWinds measurements using a least squares estimator based on data from the winter months before and after the melt season. Since the tandem dataset is short, consisting primarily of summer months, daily winter QuikSCAT-only images of Greenland from JD 001–061 and 305–365 are used to estimate σ^o_{dry}. Figure 12 shows an image for σ^o_{dry} on JD 001 and the slope of σ^o_{dry} over the winter of year 2003. The estimation of the ice-sheet summer melt produces a number of images of the ice state, the MSI, RSI and other indices.

Using the Markov melt detector, the melt season of 2003 is characterized. Figure 13 shows the first day of seasonal melt, the last day that liquid water is detected in the snow-pack, and the length of the melt season. Small melt artifacts seen in the dry snow zone are the result of noise in SeaWinds images on JD 226 and 262 due to missing backscatter data when the instrument was offline.

Most of the melt season is captured by the tandem dataset; however, there are several patches in figure 13 along the south-eastern coast near 65.0 N 42.0 W and 65.5 N 40.5 W, as well as slightly inland near 62.5 N 44 W, where melt may have started prior to the dataset, indicated by the melt starting on the first day of the dataset. Progression of the melt season across the island appears to occur regionally, and in discrete increments. For example, most of the snow-pack near the western coast begins its melt season on JD 140 and reaches far inland on the following day, JD 141, bridging the

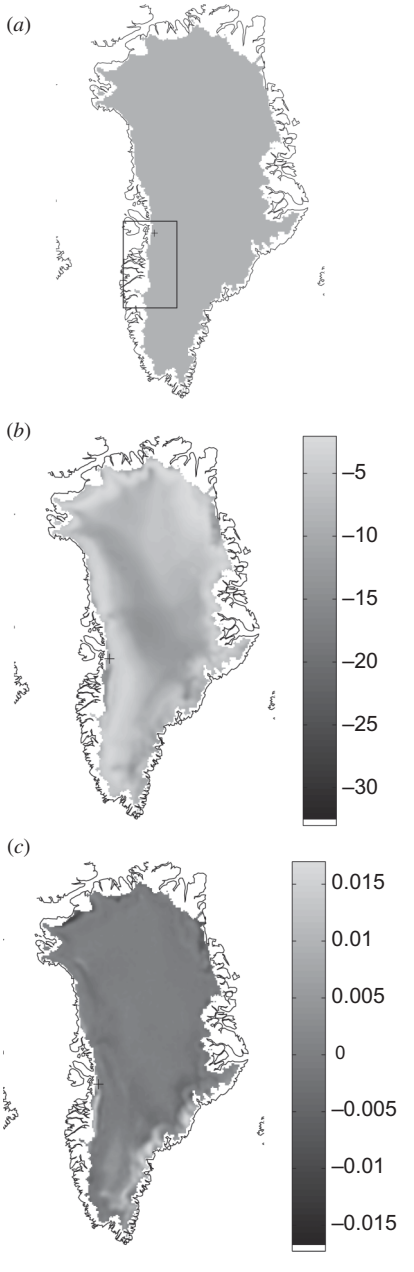

Figure 12. Tandem backscatter images. (*a*) Ice-sheet mask. (*b*) σ^o_{dry} at JD 001, 2003 in dB. (*c*) Slope of σ^o_{dry} verses time in dB per day during the winter of 2003. The cross in these and subsequent images shows the location of the ETH/CU Swiss Camp. The box shows the region used to extract the time series in figure 15.

west and east sides of the southern tip of the island near the saddle separating the summit from South Dome. The northern and northeastern coastal areas begin melt slightly later, near JD 155. Melt progresses up-slope in western Greenland into the percolation zone in several increments, JD 177, 197, 219 and 236–238. The progression

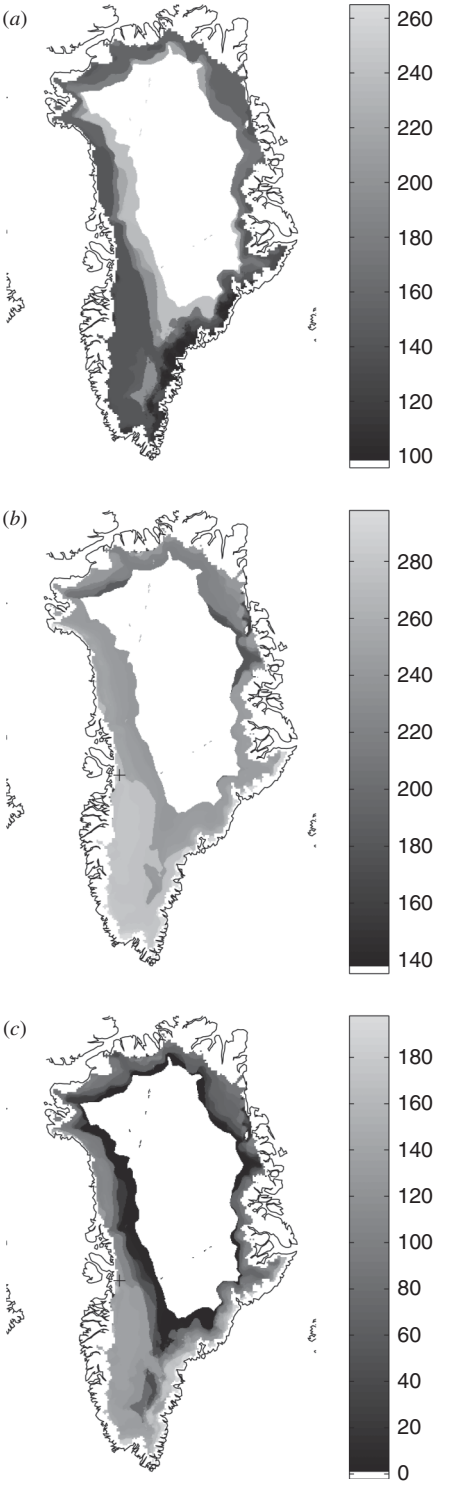

Figure 13. Seasonal melt maps. (*a*) The first day of the year 2003 in which melt is detected using tandem SeaWinds data. (*b*) The last day of the year 2003 liquid water is detected (melt or refreeze). (*c*) The length of the melt season in days.

of melt across South Dome in southern Greenland occurs in two increments: JD 151 and 197. Several pockets of melt along the eastern coast begin early, on JD 135, and progress up-slope incrementally on JD 141, 143, 159 and 173.

Like melt, seasonal refreeze indicated in figure 13 occurs regionally and in discrete increments; however, refreeze appears to spread much more quickly and uniformly than melt. The higher elevation percolation regions of southern and western Greenland finish refreezing on JD 239. Refreeze progresses nearly to the edge of the ice-sheet along the western coast by JD 250. A late season melt event caused by the remnants of Hurricane Juan leaves the snow pack wet in southern Greenland until JD 276–278. Northern and northeastern Greenland refreeze much sooner, beginning along the coastal region near 76.5 N 23.5 W on JD 157. Refreeze occurs in the north and northeastern percolation zones starting JD 180 and progresses completely to the edge of the ice-sheet by JD 222. A very small region near the southern tip of the island shows continued melt up to the last day in the tandem dataset, JD 297. Thus, the last day of melt may be later than shown at this location.

The season length shown in figure 13 suggests the season length is regionally correlated and varies from region to region. The longest melt season occurs where the first melt is detected in pockets along the southeastern coast and the southern tip of the island. (Because of the limited number of days in the dataset, some of these areas may have longer seasons than indicated since melting starts before the beginning of the dataset.) Besides these pockets along the southeastern coast, the snow-pack east of Jakobshavn (roughly 69.2 N 50.0 W) has the longest melt season of 179 days, followed by a strip of snow along the northern end of the Melville Bugt (around 76 N 65 W) with a season of 144 days. The vast majority of the southern and western parts of Greenland have a melt season 135–136 days long. Further north along the western coast, the season becomes shorter: 108 days. Northern and northeastern Greenland have relatively short melt seasons ranging from 60 to 90 days. Naturally, the shortest seasons are located at higher elevations, as short as a single day near the dry snow line separating the percolation and dry snow zones.

The IMSI for the ice-sheet is shown in figure 14. It is clear from this figure that the dynamic range of melt severity is quite large – over three orders of magnitude from the edge of the dry-snow zone to the edge of the wet-snow zone. Melt is greatest along the southeastern coast, in the same region where the melt season is longest. The southern and western sides of the island experience greater melt than the northern and northeastern sides – typically the IMSI is three to five times higher in southern Greenland than northern Greenland. It is interesting to note, however, that there is much greater contrast between the percolation and wet-snow regions than the melt along the edge of the ice-sheet from region to region across the island.

While melt state detection using the Markov detector appears to work well across the ice-sheet, the MSI and RSI and other severity indices are only applicable in regions where the snow-pack resembles the layered melt model. In the lower edges of the ablation zone, snow from the previous year's accumulation completely melts away, exposing the dense glacial ice beneath. Exposed glacial ice behaves markedly differently in melting conditions than snow, and invalidates the MSI and RSI in this area.

The change in behaviour of snow is seen in the IMSI shown in figure 14. In western Greenland a ridge of maximum melt severity occurs well within the edge of the ice-sheet. This peaked region likely occurs near the equilibrium line, where the previous season's melt is entirely melted away, showing a stark change in the structure

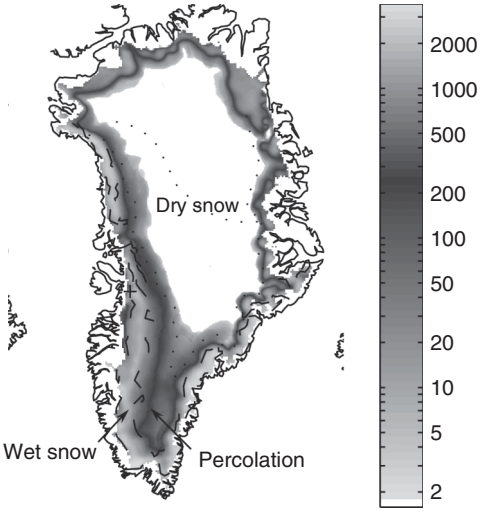

Figure 14. Seasonal IMSI, I_χ, in Np h for 2003 with key ice facies identified from 1978 Seasat scatterometer data (Long and Drinkwater 1994).

of the snow-pack, from iced-firn to glacial ice. The ridge of high IMSI appears to be near the equilibrium line due to its position relative to the ETH/CU Swiss Camp, which is near this line (see figure 14). A change in the snow characteristics, evidence for the IMSI ridge, is also seen in the backscatter at the ETH Camp shown in figure 7; beyond JD 200, the backscatter is always higher before JD 200, even during the heat wave starting on JD 235, when the highest temperatures of the season are observed.

To gain further insight into the ridge of maximum IMSI observed in western Greenland seen in figure 14, the MSI and RSI time series are analysed. Figure 15 shows a series of morning ME, $\chi - \xi$, images of a section of Greenland. Only morning images are shown for reasons of brevity. Days not shown in these figures do not have significant persistent melt and are omitted. The morning images, which exhibit persistent melt, reveal some interesting behaviour. A strip of persistent melt appears in these image some distance from the western edge of the ice-sheet. Moreover, this strip slowly moves eastward as the melt season progresses. From this it can be postulated that this persistent melt strip identifies saturated wet snow. Furthermore, the western edge of this strip identifies where the wet snow ends and the exposed glacial ice begins.

The model described previously is designed for application to firn. In order to properly deal with melting of glacial ice, a modified model is needed which can account for the differences in the melt water transport mechanism, that is, runoff versus percolation. However, dealing with rapid runoff of water along small channels in the glacial ice, rather than the more diffuse percolation assumed by the two- and three-layer models, is difficult due to the nature of localized flow, and the lack of information of its effects on backscatter. As a result, this is not attempted in this article. However, we note that identification and discrimination of ice and firn can be improved by using the MSI and RSI.

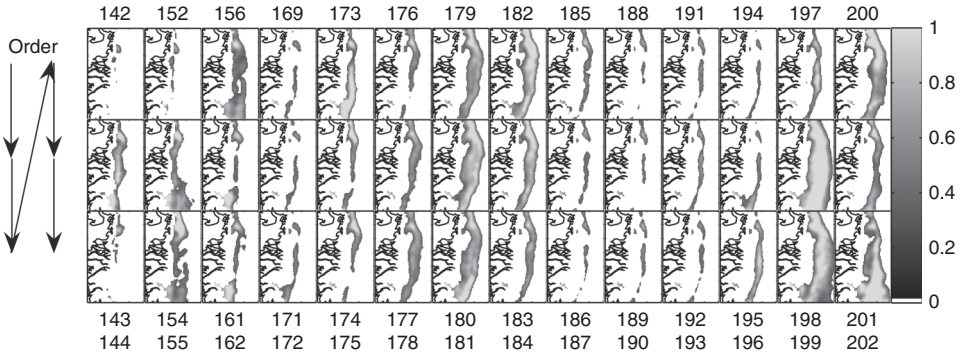

Figure 15. Time series of morning $\chi - \xi$ images over a small section of western Greenland shown in figure 12. The day of the year is specified above for the top row of images, and below for the middle and bottom row. Chronological order proceeds top to bottom, and left to right. The images illustrate the ridge of persistent melt for 2003. The region west of the melt ridge seen in figure 14 is seen in the time series as a vertical strip of persistent melt.

Figure 14 shows the IMSI with a Long–Drinkwater facies map overlay. The overlay shows the boundary of the snow zones as of the fall of 1978 (Long and Drinkwater 1994). This map was originally created by identifying differences in the backscatter across the various regions of Greenland from fall SASS data. It is clear that there is strong correlation between the map and the IMSI. While the subjective metric used to distinguish the snow zones in the 1978 map is very different from the method used to create the IMSI image, the similarities suggest that the IMSI could reasonably be used to classify the ice facies. Moreover, the IMSI could be used as an objective classifier of snow types since it attempts to measure melt directly rather than classifying snow types indirectly through changes in dry snow backscatter which may be affected by other factors.

Some of the differences between the 1978 facies map and the IMSI image shown in figure 14 are noteworthy. The most apparent difference is the line separating the percolation zone and dry snow in the 1978 map, and the location of the no-melt line in the IMSI image. Differences in the metrics used to create these two maps may explain some of the facies map and IMSI image differences; however, the IMSI along the 1978 dry snow line is typically 100 Np h. This large value cannot be explained by a solitary melt event, particularly since most of the boundary pixels experienced 5–20 days of melt in 2003. With so many days of melt observed, it is apparent that the dry snow must be further up-slope in the 2003 data than the 1978 line. Movement of the dry-snow line further up-slope is consistent with a general warming trend in western Greenland (Drinkwater and Long 1998). Further study is warranted.

4. Conclusion

Scatterometers are proven tools for detecting melt in sea ice and snow and the long time series of scatterometer data can be used to support climate change studies. Though short-lived, the SeaWinds tandem mission provides a valuable dataset capable of resolving the diurnal cycle in Greenland.

This article represents a first step towards exploiting this dataset to attempt to recover estimates of the severity of Greenland melt from active microwave data. The

models and methods used in this article are simplistic and thus have limitations. However, at the coarse scale of the scatterometer observations they work surprisingly well for this initial study and provide insight into the seasonal melt cycle of the Greenland ice-sheet. It is hoped that this work will encourage additional research in the applications of scatterometer data to melt severity estimation.

Acknowledgements

SeaWinds data was obtained from the Jet Propulsion Laboratory Physical Oceanography Distributed Active Archive (podaac.jpl.nasa.gov). Tandem Greenland local time-of-day images were provided by the Scatterometer Climate Data Record Pathfinder (www.scp.byu.edu).

References

Abdalati, W. and Steffen, K., 1995, Passive microwave-derived snow melt regions on the Greenland ice sheet. *Geophysical Research Letters*, **22**, pp. 787–790.

Abdalati, W. and Steffen, K., 1997, Snowmelt on the Greenland ice sheet as derived from passive microwave satellite data. *Journal of Climate*, **10**, pp. 165–175.

Ashcraft, I.S. and Long, D.G., 2005, Differentiation between melt and freeze stages of the melt cycle using SSM/I channel ratios. *IEEE Transactions on Geoscience and Remote Sensing*, **43**, pp. 1317–1323.

Ashcraft, I.S. and Long, D.G., 2006a, Comparison of methods for melt detection over Greenland using active and passive microwave measurements. *International Journal of Remote Sensing*, **27**, pp. 2569–2488.

Ashcraft, I.S. and Long, D.G., 2006b, Relating microwave backscatter azimuth modulation to surface properties of the Greenland ice sheet. *Journal of Glaciology*, **52**, pp. 257–266.

Benson, C.S., 1962, Stratigraphic studies in the snow and firn of the Greenland ice sheet. SIPRE Research Report.

Colbeck, C.S., 1979, Waterflow through heterogeneous snow. *Cold Region Science and Technology*, **1**, pp. 37–45.

Drinkwater, M.R. and Long, D.G., 1998, *Seasat, ERS-1/2 and NSCAT Scatterometer Observed Changes on the Large Ice Sheets* (Noordwijk, The Netherlands: ESA SP-424, ESA Publications Div., ESTEC).

Early, D.S. and Long, D.G., 2001, Image reconstruction and enhanced resolution imaging from irregular samples. *IEEE Transactions on Geoscience and Remote Sensing*, **39**, pp. 291–302.

Flach, J.D., Partington, K.C., Ruiz, C., Jeansou, E. and Drinkwater, M.R., 2005, Inversion of the surface properties of ice sheets from satellite microwave data. *IEEE Transactions on Geoscience and Remote Sensing*, **43**, pp. 743–752.

Gallée, H. and Duynkerke, P., 1997, Air–snow interactions and the surface energy and mass balance over the melting zone of West Greenland during GIMEX. *Journal of Geophysical Research*, **102**, pp. 13 813–13 824.

Greuell, W. and Konzelmann, T., 1994, Numerical modelling of the energy balance and the englacial temperature of the Greenland Ice Sheet. Calculations for the ETH-Camp location (Western Greenland, 1155 m a.s.l.). *Global Planetary Change*, **9**, pp. 91–114.

Hicks, B.R., 2006, Melt detection and estimation in Greenland using Tandem SeaWinds and QuikSCAT Scatterometers, Master's thesis, Brigham Young University, Provo, UT.

Hicks, B.R. and Long, D.G., 2006, Diurnal melt detection on Arctic sea ice using Tandem QuikSCAT and SeaWinds data. In *Proceedings of the IEEE International Geoscience and Remote Sensing Symposium*, August (Denver, CO: IEEE), pp. 4112–4114.

Jordan, R., 1992, A one-dimensional temperature model for a snow cover: Technical documentation for SNTHERM.89. CRREL Special Report.

Kunz, L.B. and Long, D.G., 2006, Melt detection in Antarctic ice-shelves using spaceborne scatterometers and radiometers. *IEEE Transactions on Geoscience and Remote Sensing*, **44**, pp. 2461–2469.

Lefebre, F., Gallée, H., van Ypersele, J.P. and Greuell, W., 2003, Modeling of snow and ice melt at ETH Camp (West Greenland): a study of surface albedo. *Journal of Geophysical Research*, 4231, doi:10.1029/2001JD001160.

Long, D.G. and Drinkwater, M.R., 1994, Greenland ice-sheet surface properties observed by the Seasat-A Scatterometer at enhanced resolution. *Journal of Glaciology*, **40**, pp. 213–230.

Mätzler, C., 1994, Passive microwave signatures of landscapes in winter. *Meteorology and Atmospheric Physics*, **54**, pp. 241–260.

Nghiem, V.S., Steffen, K., Kwak, R. and Tsai, W.Y., 2001, Detection of snowmelt regions on the Greenland ice sheet using diurnal backscatter change. *Journal of Glaciology*, **47**, pp. 539–547.

Rowe, C.M., Kuivinen, K.C. and Jordan, R., 1995, Simulation of summer snowmelt on the Greenland ice sheet using a one-dimensional model. *Journal of Geophysical Research*, **100**, pp. 16 265–16 273.

Steffen, K., Box, J.E. and Abdalati, W., 1996, Greenland Climate Network: GC-Net. *CRREL Special Report on Glaciers, Ice sheets and Volcanoes*, **96-27**, pp. 98–103.

Sturm, M., 1997, The thermal conductivity of seasonal snow. *Journal of Glaciology*, **43**, pp. 26–41.

Ulaby, F., Moore, R. and Fung, A., 1986, *Microwave Remote Sensing: Active and Passive*, Vol. 2 (Norwood, MA: Artech House).

Ulaby, F., Moore, R. and Fung, A., 1990, *Microwave Remote Sensing: Active and Passive*, Vol. 3 (Norwood, MA: Artech House).

Wismann, V., 2000, Monitoring of seasonal snowmelt on Greenland with ERS Scatterometer data. *IEEE Transactions on Geoscience and Remote Sensing*, **38**, pp. 1821–1826.